Case Study

Progressive Collapse Behavior of a Long-Span Cable-Stayed Bridge Induced by Cable Loss

Qian Chen, Ph.D., M.ASCE[1]; Hongfan Wang[2]; Sherif El-Tawil, F.ASCE[3]; Anil K. Agrawal, Dist.M.ASCE[4]; Baidurya Bhattacharya, F.ASCE[5]; and Waider Wong[6]

Abstract: Driven by high-profile events, much attention has been paid to the progressive collapse behavior of building structures. Comparably less research has addressed bridges, especially long-span cable-stayed bridges. In this paper, the progressive collapse behavior of a prototype long-span cable-stayed bridge is computationally investigated through stay-cable removal analyses. The simulations are carried out by direct sudden removal of a single stay cable at different locations and sequential removal of multiple cables. Dynamic effects as well as material and geometric nonlinearities are accounted for in the simulations, which are used to investigate critical cable loss locations and system response to the various cable loss scenarios. The simulation results show that the prototype bridge exhibits good robustness against failure of a single stay cable. When multiple cables are removed, the bridge is less tolerant to cable losses near its supporting pylons than its midspan. For the former, it exhibits an instability-type partial collapse as opposed to an unzipping type of progressive collapse followed by pylon failure for the latter. **DOI: 10.1061/JBENF2.BEENG-5840**.

Author keywords: Progressive collapse; Cable-stayed bridge; Cable loss; Finite-element model; Nonlinear dynamic analysis.

Introduction

Cable-supported bridges, such as tied-arch bridges, cable-stayed bridges, and suspension bridges, are widely used around the world. As the name implies, cables are key structural components of cable-supported bridges. Cables are vulnerable to damage and even failure due to various reasons, such as corrosion as in Nanfang'ao Bridge (TTSB 2020), fatigue, a combination of corrosion and fatigue, fire as in the Rio-Antirrio and Mezcala bridges (Zoli and Steinhouse 2007), blast, vehicle or vessel impact as in the Qingzhou Bridge (Zoli and Steinhouse 2007), and improper design as in the Kutai Kartanegara Bridge (Kawai et al. 2014). Although cable damage is local, it could progress into a partial or complete failure of the entire bridge structural system. This type of structural response, if it occurs, is termed "progressive collapse" (GSA 2003; Khandelwal et al. 2008a, b; Bao et al. 2008; DOD 2009).

Cable loss analysis is generally used to assess the potential for progressive collapse. Guidelines for cable-stayed bridges [e.g., PTI (2007) and Eurocode 3 (CEN 2006)] recommend using a dynamic amplification factor (DAF) within a static analysis framework to consider accidental cable loss. Hyttinen et al. (1994) studied the DAF of the Saame Bridge due to sudden failure of a single cable and found that the maximum DAF was 1.8. Wolff and Starossek (2010) investigated single cable loss in a five-span cable-stayed bridge and found that the DAF varied within a wide range for different types of structural members. Mozos and Aparicio (2010a, b) also performed detailed analysis of the dynamic behavior of cable-stayed bridges subjected to sudden cable loss and found that the DAF varied for different layouts of stays. Aoki et al. (2013) investigated both the DAF adopted by Wolff and Starossek (2010) and the equivalent DAF by Zoli and Woodward (2005) and found that DAF values were over 2.0 for the bending moment and axial force at different sections along the deck, towers, and cables while their demand to capacity ratio (DCR) remained below 1. Similar work was also conducted by Kao and Kou (2010) and Zhou and Chen (2015), with a focus on the dynamic behavior of bridges under the loss of single to three cables. However, the potential for progressive collapse was not studied. Cai et al. (2012) compared the analysis approaches for the progressive collapse of cable-stayed bridges and concluded that nonlinear dynamic analysis is the best method to trace the collapse progression after an initial loss of one or more cables.

As already discussed, research results on the progressive collapse behavior of cable-stayed bridges due to cable loss are limited, especially those that tracked the progressive collapse process all the way to complete failure. Existing studies are also conflicting in some cases. For example, while Wolff and Starossek (2010) suggested that near-pylon cables are more critical to collapse resistance than cables that are farther out, Das et al. (2016) indicated the opposite. Given the dearth of information on this topic, the main objective of this paper is to contribute to the state of the art by studying the dynamic behavior and potential progressive collapse behavior of cable-stayed bridges due to single or multiple cables loss scenarios. An existing long-span cable-stayed bridge is

[1]Dept. of Civil and Environmental Engineering, The City College of New York, New York, NY 10031 (corresponding author). ORCID: https://orcid.org/0000-0002-8651-5210. Email: chenqian022@hotmail.com

[2]Postdoctoral Researcher, Dept. of Civil and Environmental Engineering, The City College of New York, New York, NY 10031. ORCID: https://orcid.org/0000-0001-6854-511X. Email: hwang2@ccny.cuny.edu

[3]Antoine E. Naaman Collegiate Professor of Civil and Environmental Engineering, Dept. of Civil and Environmental Engineering, Univ. of Michigan, Ann Arbor, MI 48105. Email: eltawil@umich.edu

[4]Herbert G. Kayser Professor of Structural Engineering, Dept. of Civil and Environmental Engineering, The City College of New York, New York, NY 10031. Email: agrawal@ccny.cuny.edu

[5]Professor, Dept. of Civil Engineering, Indian Institute of Technology Kharagpur, Kharagpur, WB 721302, India. ORCID: https://orcid.org/0000-0002-8758-7486. Email: baidurya@civil.iitkgp.ac.in

[6]Engineer, Federal Highway Administration, Baltimore, MD 21201. Email: waider.wong@dot.gov

Note. This manuscript was submitted on May 5, 2022; approved on May 19, 2023; published online on July 13, 2023. Discussion period open until December 13, 2023; separate discussions must be submitted for individual papers. This paper is part of the ***Journal of Bridge Engineering***, © ASCE, ISSN 1084-0702.

selected as a prototype bridge and a three-dimensional (3D) explicit finite-element model (FEM) with material nonlinearity and predefined failure criteria is developed to perform the collapse simulations and investigate collapse behavior.

Cable-Stayed Bridge Prototype and FEM

The selected example bridge has a total length of 1,004.6 m. It consists of one 471.2 m main span, two 198.1 m side spans, and two 68.6 m approach side spans on both sides. Carrying two-way traffic, the bridge has four vehicular lanes in each direction plus one walkway on the south side. The total width of the bridge deck is 42.7 m in the main and long side spans. The width changes to 36.6 m in the approach side spans. The diamond-shape pylons are 175 m high and are connected to the girders by 64 stayed cables in each plane. All cables are regularly spaced at 14.3 m along the deck, except for the first and the last four back stays in the side spans.

FEM

A 3D FEM of the selected bridge was developed to run on the LS-DYNA platform (LSTC 2020), as shown in Fig. 1. The explicit analysis capabilities provided by LS-DYNA are preferable when dealing with scenarios that entail highly nonlinear material behavior, large deformations, contact, and rapid load application (e.g., associated with sudden member loss). The FEM accounts for the stay cables, bridge pylons, piers, girder members, floor beams, stringers, diaphragms, secondary bracing members, concrete deck, elastomeric bearings, and nonstructural components. Table 1 summarizes the element types and material models used to model the different structural components of the bridge, and Table 2 summarizes the material properties of each structural components. Overall, the FEM consisted of 12,968 nodes, 6,039 beam elements, 1,872 shell elements, 1,611 mass element, and 2,132 nodal rigid bodies. The detailed material nonlinearity considerations for each of the structural components are introduced in the following subsections.

Structural Steel Members

Structural steel components, including girder members, floor beams, stringers, steel diaphragms, and secondary bracing members were modeled by Hughes–Liu beam elements with cross-section integration. Approximately 20 to 30 integration points were used for each section, depending on the section shape. The material nonlinear behavior of these components was modeled

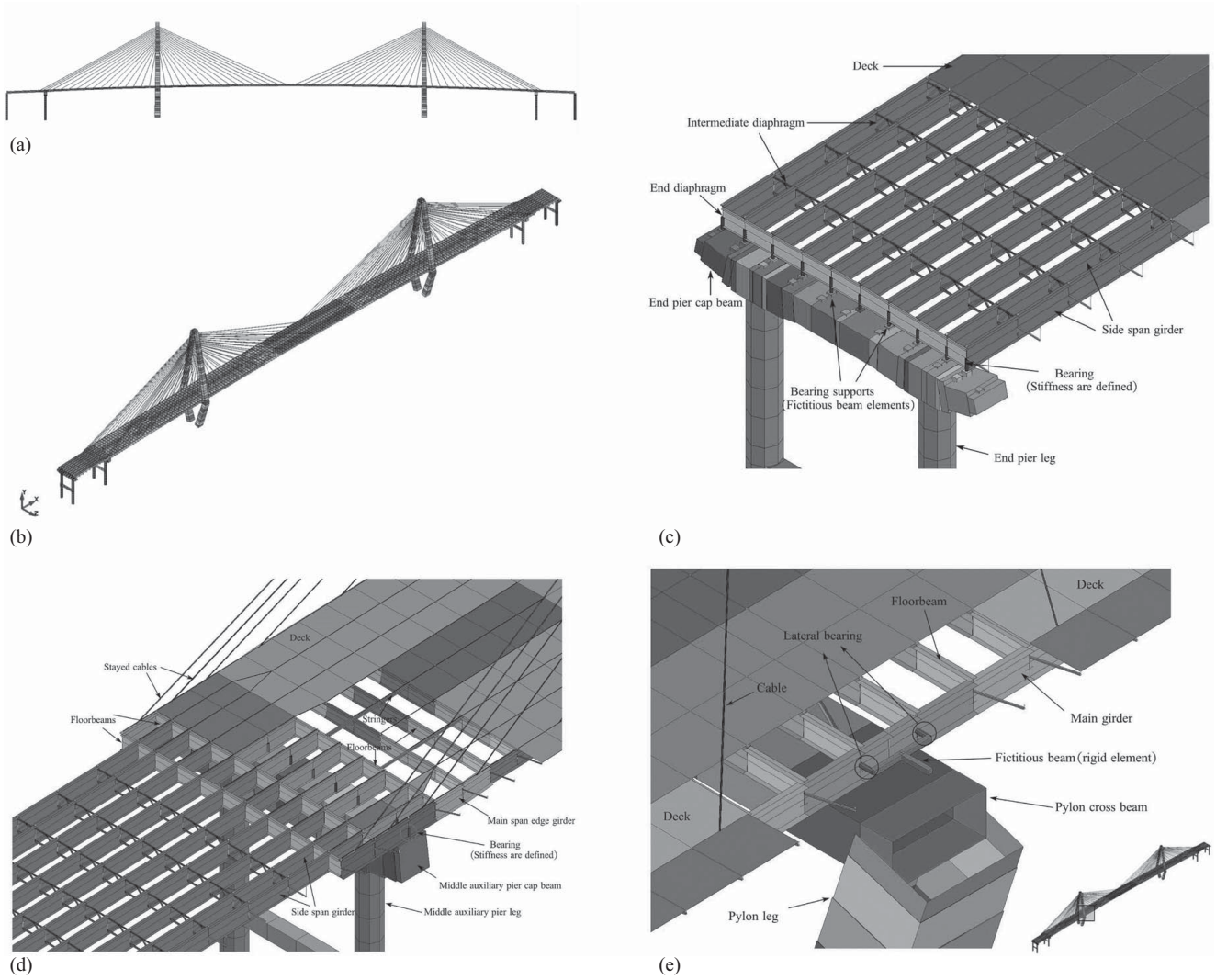

Fig. 1. FEM of the prototype bridge: (a) elevation view; (b) isometric view; (c) components information near end pier; (d) components information near middle auxiliary pier; and (e) components information near pylon leg.

Table 1. Element and material information for the FEM of the prototype bridge

Structural members	Element types	Material information
Stay cables	Multiple truss elements	*MAT_PLASTIC_KINEMATIC
Substructure (bridge pylons, piers)	Belytschko–Schwer resultant beam	*MAT_MOMENT_CURVATURE_BEAM
Structural steel member (e.g., girder, floor beam, stringer)	Hughes–Liu beam with cross-section integration	*MAT_PLASTIC_KINEMATIC
Concrete deck	Fully integrated shell element	*MAT_PLASTICITY_COMPRESSION_TENSION
Bearings	Discrete beam element	*MAT_NONLINEAR_ELASTIC_DISCRETE_BEAM
Miscellaneous connection	N/A	*CONSTRAINED_NODAL_RIGID_BODY
Nonstructural elements (e.g., barrier)	Mass element	N/A
Support on substructures	Belytschko–Schwer resultant beam	*MAT_RIGID

Table 2. Material properties of structural components in the prototype bridge

Structural components	Materials	Young's modulus (GPa)	Compressive strength (MPa)	Yield strength (MPa)	Ultimate strength (MPa)	Failure strain
Pylons and piers	Concrete	32.88	48.26	—	—	—
Deck	Concrete	35.15	55.16	—	—	—
Reinforcing Steel	ASTM A615 Grade 60	200	—	413.7	620.5	0.2
Posttensioning strands	AASHTO M203 Grade 270	196.5	—	1,689.9	1,861.6	0.06
Stay cables	ASTM A416 Grade 270	196.5	—	1,689.9	1,861.6	0.06
Girders, floor beams, stringers, and others	AASHTO M270 Grade 50	200	—	344.7	448.2	0.2

by the *MAT_PLASTIC_KINEMATIC (MAT_003) material model. This material model is cost effective and provides an elastoplastic behavior with kinematic hardening behavior as shown in Fig. 2. The element was automatically deleted if the strain in the element reached the defined ultimate strain (20%), which was selected based on guidance in Khandelwal et al. (2008a).

Bridge Pylon

The bridge pylon legs are primarily subjected to biaxial bending moments and axial force during a member loss scenario. To avoid the complexity of modeling detailed reinforcement explicitly, while considering the interaction between axial forces and bending moments, the material nonlinearity of the reinforced concrete bridge pylon was characterized by a simplified model *MAT_MOMENT_CURVATURE_BEAM (MAT_166) with Belytschko–Schwer beam elements. In this formulation, different user-defined moment curvatures can be provided as a function of axial force level and a failure criterion could be set up based on the ultimate curvature at each section.

The modeling approach is demonstrated by comparing simulation results with test results in the literature. Vecchio and Shim (2004) conducted a series of beam tests to investigate the behavior of reinforced concrete elements. In these tests, simply supported beams with a span length of 6,400 mm were pushed down by a centerpoint load with a servocontrolled MTS universal testing machine, as shown in Fig. 3. Test cases A3 and B3 were selected for comparison. The section details and material information for this test setup are provided in Fig. 4 and Table 3 (Vecchio and Shim 2004).

The two beams (Case A3 and B3) were modeled by using the aforementioned modeling scheme. A separate section analysis was also conducted to compute the moment curvature curves under axial loads that ranged from the section's axial tensile capacity to its axial compression capacity. Twelve moment curvature curves under six different axial forces were selected as the input data for the material model for each case, as presented in Table 4 and Figs. 5 and 6. Pushdown analysis of these two beams were conducted

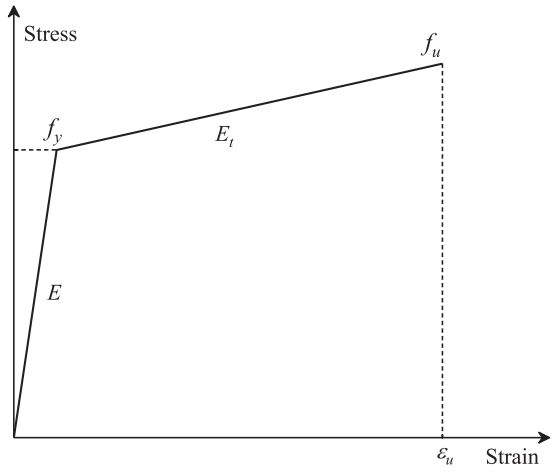

Fig. 2. Material model of structural steel members.

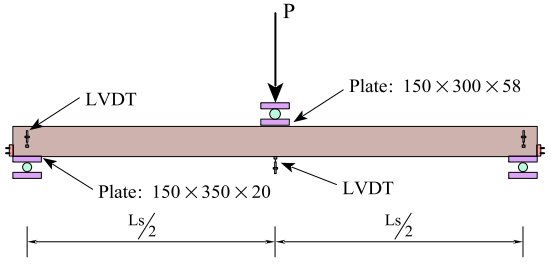

Fig. 3. Test setup (Case A3 and B3) (unit: mm). (Data from Vecchio and Shim 2004, © ASCE.)

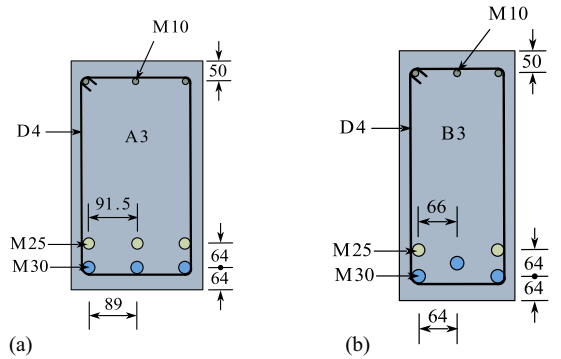

Fig. 4. Cross-section details of test beams (unit: mm): (a) Case A3; and (b) Case B3. (Data from Vecchio and Shim 2004, © ASCE.)

Table 3. Material properties of the test beams

Reinforcement				
Bar size	Area (mm^2)	f_y (MPa)	f_u (MPa)	Es (MPa)
M10	100	315	460	200,000
M25	500	445	615	220,000
M30	700	436	700	200,000
Concrete				
Test beam	f'_c (MPa)	f'_{sp} (MPa)	ε_0 (mm/mm)	Ec (MPa)
A3	43.5	3.13	0.0019	34,300
B3	43.5	3.13	0.0019	34,300

Table 4. Axial forces information for input data of the moment curvature curves (unit: kN)

Axial force	N1	N2	N3	N4	N5	N6
Case A3	−3,892.2	−2,918.9	−1,946.6	−973.2	0.0	841.4
Case B3	−3,001.3	−2,251.1	−1,500.3	−550.7	0.0	27.7

by applying *BOUNDARY_PRESCRIBED_MOTION_NODE at the center nodes of the test beams. The comparisons of load displacement curves obtained from the test results (long dashed line labeled as A3_Test and B3_Test) and simulations (solid line labeled as LS-DYNA) are shown in Fig. 7. It is observed from this figure that the selected modeling scheme is able to accurately simulate the strength, deflection at failure for B3, and, to a lesser extent, the initial stiffness.

Stay Cables

There are 128 cables with different cross-section areas and pretensioning forces in the bridge. The stay-cables consist of 15.7 mm diameter uncoated, seven wire, weldless, low-relaxation strands complying with the requirements of ASTM A416, Grade 270. According to AASHTO LRFD Bridge Design Specifications (AASHTO 2020), the elastic modulus (Es) is 196,500 MPa and the tensile strength (f_u) is 1,860 MPa with ultimate strain (ε_u) of 6%. The yield strength (f_y) is 90% of the tensile strength (f_u) for the cables. Each cable was modeled with 10 truss elements in order to accurately represent the sag effect. Material nonlinear response was modeled by the *MAT_PLASTIC_KINEMATIC (MAT_003) material model. The input parameters for this model are shown in Table 5. The element was automatically deleted when the strain in cable elements reached 6%, which is a typical failure strain for Grade 270 steel strands. The ADD_THERMAL_EXPANSION option was used to give MAT_003 a thermal expansion capability. The pretensioning forces based on the design calculations were applied as an equivalent thermal load (achieved by decreasing the temperature in stayed-cable elements) during a 0.1 second period by using the command *LOAD_THERMAL_CONSTANT_NODE.

Bridge Deck and Posttensioning Strands

The bridge deck was modeled by using fully integrated four-node, isotropic shell elements. The bridge deck was connected to the underlying steel girder members and floor beams though rigid links using *CONSTRAINED_NODAL_RIGID_BODY. To avoid the complexity of modeling detailed reinforcement explicitly, the material nonlinearity of the bridge deck was considered by a simplified model introduced and calibrated by Alashker et al. (2011). This simplified model emphasizes the tensile membrane response of the concrete deck since its flexural resistance becomes insignificant at large deformation levels near the ultimate states. The uniaxial material response was based on the following assumptions: (1) the concrete slab is the only source for compressive resistance, and it has zero tensile strength; and (2) the steel reinforcement mesh is the only source of tensile resistance. The Kent and Park Model (1971) was employed for the nonlinear stress–strain relationship for concrete in compression. The equivalent tensile

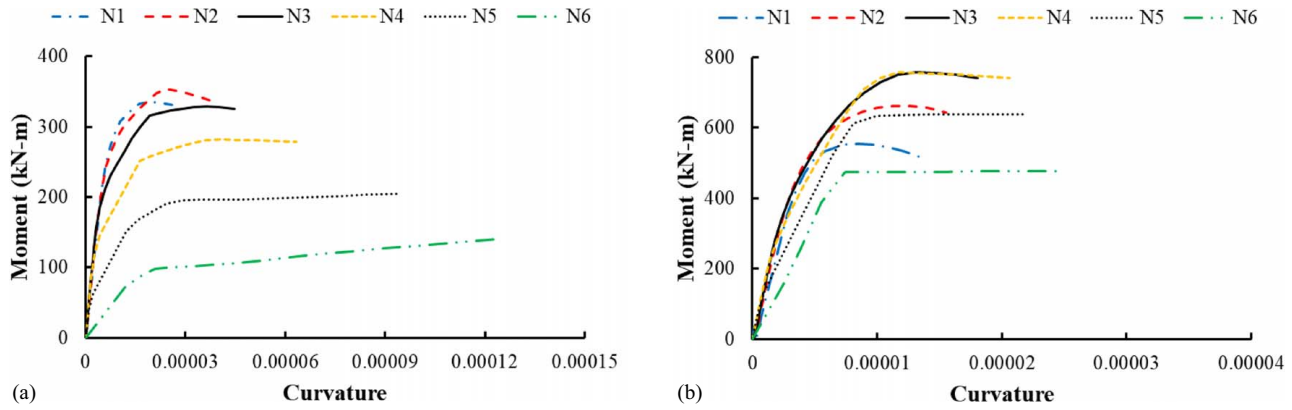

Fig. 5. Moment curvature curves under different axial forces of Case A3: (a) moment curvature curves about weak axis; and (b) moment curvature curves about strong axis.

J. Bridge Eng., 2023, 28(9): 05023005

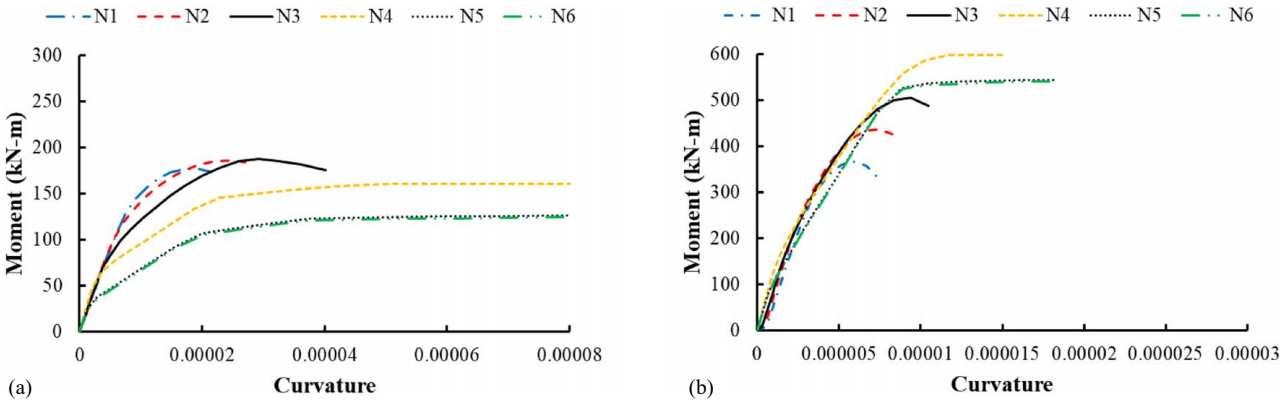

Fig. 6. Moment curvature curves under different axial forces of Case B3: (a) moment curvature curves about weak axis; and (b) moment curvature curves about strong axis.

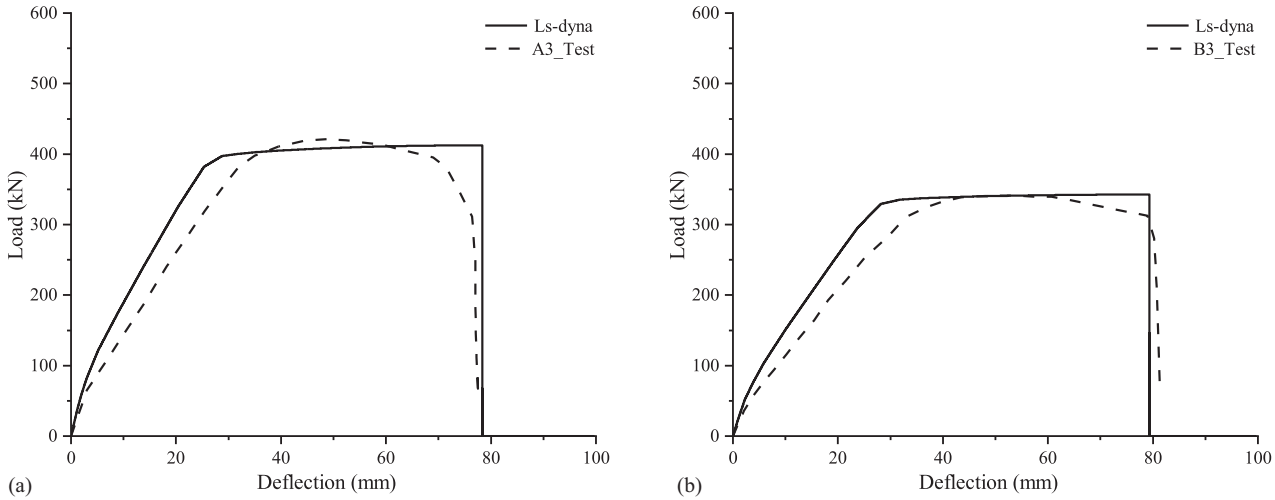

Fig. 7. Load–Displacement responses: (a) Case A3; and (b) Case B3.

Table 5. Input parameters for MAT_003 (Cable ASTM A416 Grade 270)

f_y	E_t	Es	Ultimate strain (ε_u)
1,675.4 MPa	3,613.3 MPa	196,500 MPa	6%

stress–strain relationship due to reinforcement was defined by

$$F_{t,eq}(\varepsilon) = \frac{F_{t,R}(\varepsilon)A_R}{A_{eq}} \tag{1}$$

where $F_{t,eq}(\varepsilon)$ = equivalent tensile stress at strain ε; A_{eq} = equivalent area of the concrete shell element per unit width; $F_{t,R}(\varepsilon)$ = stress values in the steel reinforcement mesh at strain ε; and A_R = area of the mesh reinforcement per unit width. This equivalent behavior was implemented by *MAT_PLASTICITY_COMPRESSION_TENSION (MAT_124), which can model distinct tension and compression relationships. The typical stress–strain relationship of the composite deck model is shown in Fig. 8.

Posttensioning strands were used at the center of the main span and near the middle auxiliary piers in order to prevent cracking in the concrete deck. In the FEM, these posttensioning strands were modeled by truss elements with *MAT_PLASTIC_KINEMATIC (MAT_003). These elements shared common nodes with the adjacent shell elements of the concrete bridge deck. A

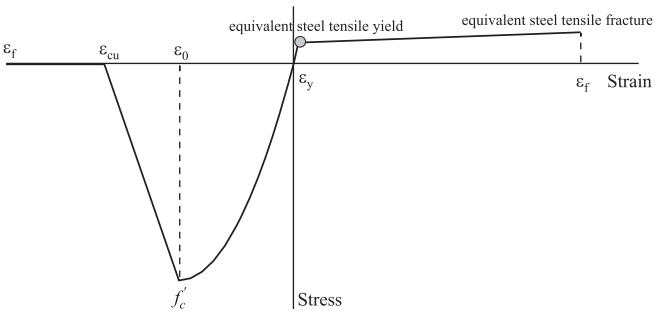

Fig. 8. Equivalent stress–strain relationship of deck elements.

close-up view of the bridge deck with posttensioning strands is shown in Fig. 9. Like the stayed-cables, thermal expansion was also considered in the material model by the ADD_THERMAL_EXPANSION option. Prestressing was induced by cooling the posttensioning strands, which thermally shrank to induce prestressing forces. The temperature change was determined by jacking forces in the design drawings, with 103 MPa prestress loss as per the Post-tensioning Manual by PTI (2006) for low-relaxation grade 270 strand in slabs. The shell element was automatically deleted if the tensile strain reached ε_f or the compressive strain reached ε_{cu}.

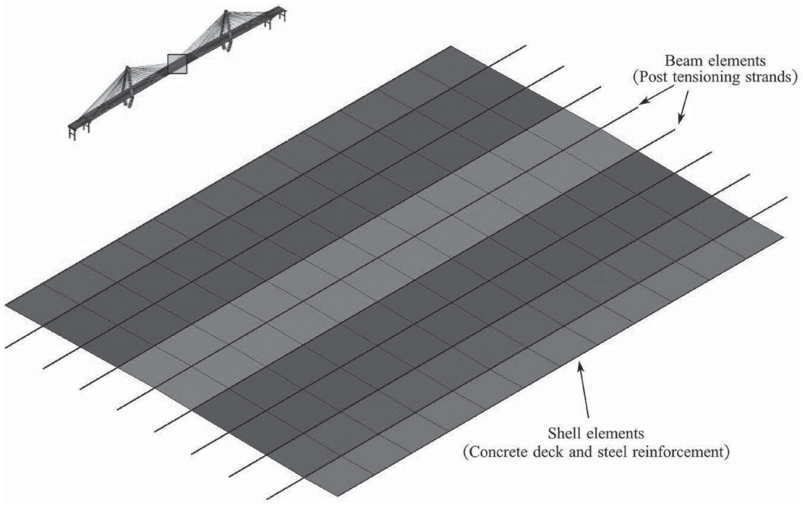

Fig. 9. Bridge deck model with posttensioning strands.

Elastomeric Bearings

The main girder members are connected to the bridge pylon legs by two lateral bearings at each leg (Fig. 10). These lateral bearings are modeled by discrete beam elements with MAT_067 (*MAT_NONLINEAR_ELASTIC_DISCRETE_BEAM). The translational stiffness and ultimate deformation for each lateral bearing are based on the design information listed in Table 6. Rotational restraints are released, so failure of each lateral bearing element is assumed to be based on the force and displacement resultants as follows:

$$\left(\frac{F_r}{F_r^{\text{fail}}}\right)^2+\left(\frac{F_s}{F_s^{\text{fail}}}\right)^2+\left(\frac{F_t}{F_t^{\text{fail}}}\right)^2 \geq 0 \tag{2}$$

$$\left(\frac{u_r}{u_r^{\text{fail}}}\right)^2+\left(\frac{u_s}{u_s^{\text{fail}}}\right)^2+\left(\frac{u_t}{u_t^{\text{fail}}}\right)^2 \geq 0 \tag{3}$$

where F_r, F_s, and F_t = force resultants along the local r-, s-, and t-axes corresponding to relative displacements u_r, u_s, and u_t, respectively; and F_r^{fail}, F_s^{fail}, F_t^{fail} = ultimate force resultants along the local r-, s-, and t-axes corresponding to failure displacements u_r^{fail}, u_s^{fail}, and u_t^{fail}, respectively. The discrete element representing the bearing is deleted if either one or both of the preceding criteria are satisfied (to represent bearing failure).

Validation and Model Limitations

It is not possible to validate the overall bridge model discussed previously because there are no available tests results of a full cable-stayed bridge system. In simulation, it is common to accept system-level results as being reasonably representative of reality when the performances of the various components have been separately validated. In addition to the validation study discussed earlier,

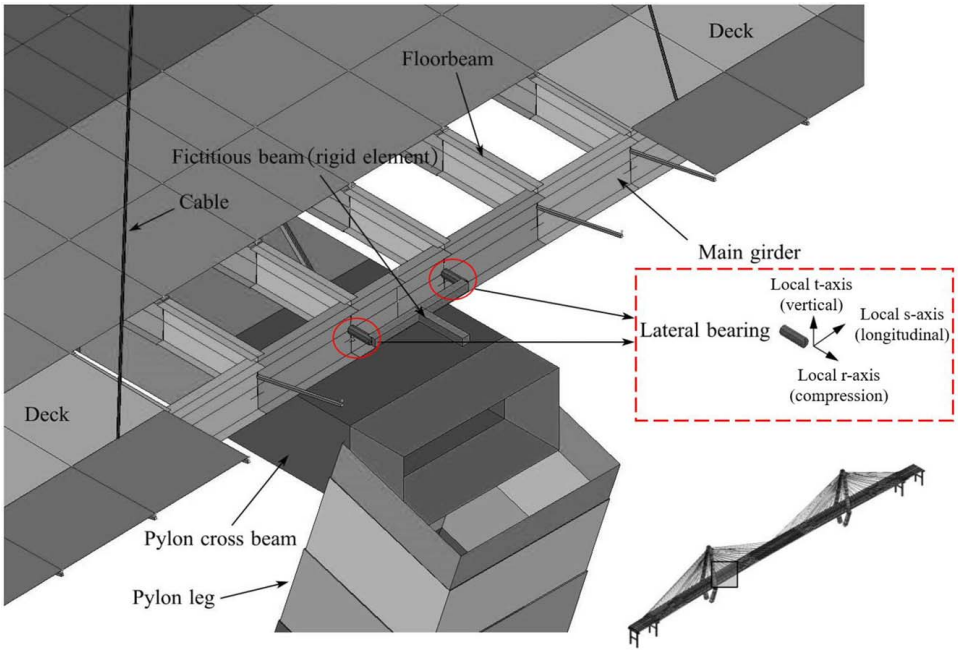

Fig. 10. Lateral elastomeric bearings connecting girder members to pylons.

Table 6. Stiffness and ultimate deformations of the lateral elastomeric bearings

Global direction	Longitudinal	Vertical	Compression
Stiffness	3.347 kN/mm	7.147 kN/mm	108.987 kN/mm
Ultimate deformation	0.905 m	0.492 m	0.075 m

Alashker et al. (2011) validated the deck model used herein. The authors have also successfully validated and utilized many of the other models discussed in this paper; for example, in Khandelwal et al. (2008b). They have also extensively worked with and validated other complex bridge models (e.g., Cao et al. 2020a, b), using the same overall modeling strategy employed herein. One limitation of the modeling scheme employed in this paper is that joint and connection responses were not modeled, such as the connections between stay cables and the girder or pylon and the moment connections between the floor beam and main girder. In essence, it is assumed that member failure will occur prior to joint failure and that joint nonlinearity will not contribute substantially to the bridge response. This is a common assumption in bridge models of the sort discussed herein. To substantiate this assumption, a comparison was conducted between the design capacity of connections and the design capacity of individual members within the context of the example bridge presented. Connor et al. (2018) also indicated in NCHRP 883 that connection failure need not be modeled if the capacity of the connections were determined to be larger than the individual member. In addition, dead load (DL) analysis and modal analysis of the prototype bridge were also conducted by using an implicit FE model in Agrawal et al. (2022, in the press). The simulation results of the explicit FE model in this paper were compared with those from the implicit FE model, showing good agreement between the two FE models.

Dead and Live Load Analysis

The construction of the bridge involved multiple stages and sequences. Achieving the same construction sequence in the FEM as in the real structure is difficult and would require significant simulation time. Hence, the DL analysis was simplified in the FEM. The initialization of the DL condition was conducted through Stages 1 and 2, and the live load was applied at Stage 3 after the bridge reached the equilibrium state under the DL:

Stage 1 (Simulation time $t = 0$–8 s): pretension forces in the cables and self-weight of the main structures were applied in this stage. A global damping of 80% of critical was applied to prevent excessive vibrations associated with sudden application of the DLs. According to the construction plans, posttensioning in the deck was applied once the deck was completed. Hence, the posttensioning strands did not contribute to stiffness during this stage therefore Young's modulus (Es) of the strands was reduced to 5% of its normal value to reflect this condition.

Stage 2 ($t = 8$–20 s): the stiffness of the posttensioning strands was increased to its normal value and the posttensioning forces were then applied. This stage was also accompanied by large global damping (80% of critical damping) to prevent numerical problems associated with excessive vibrations and shortening of the posttensioning strands.

Stage 3 ($t = 20$–30 s): after completion of Stages 1 and 2, live load was applied in this stage. This stage was also accompanied by large global damping (80% of critical damping) to prevent any spurious failure modes due to large vibrations when the live loads were applied.

Various distributions of design live load were discussed in Agrawal et al. (2022, in the press), and the results showed the one with live load distributed along the entire length of the bridge (Fig. 11) is generally the most critical for overall bridge behavior. Thus, it was selected to be presented in this paper. The simulation results of the bridge under DL only and DL plus live load (DL + LL) are introduced in the following subsection, and they were extracted at the end of Stage 2 and Stage 3 after the bridge reached its equilibrium state.

Vertical Displacements

The vertical deflection along the main girder is shown in Fig. 12. The deflection was measured from the initial camber position of the girder. Under DL, the maximum downward deflection was located at the center with a value equal to 0.427 m. The main girder near the two pylons suffered an upward displacement of 0.076 m. Under DL + LL, the maximum vertical downward displacement in the center span increased by 0.579 m compared with that for the DL condition. However, the vertical displacements in the side span for DL + LL condition remained similar to that for the DL case.

Cable Stresses

The stresses in the stay cables of the bridge are shown in Fig. 13. Under DL, the stresses in the stay cables were around 689.5 MPa. The maximum stress occurred in the longest cables at the side span and center span. The stress in the cables near the middle auxiliary pier and tower are slightly smaller than in other cables. Under DL + LL, stresses in the different cables increased in the range of 61.4 to 106.9 MPa with respect to those under DL.

Member Naming Scheme

Taking advantage of the geometric and loading symmetries, the removed cables were all located in Zone 3 in the south plane, attached to the west pylon (designated S.01 to S.32, increasing from West to East) as shown in Fig. 14. Cables in the bridge are categorized into four zones: Zone 1 with cables N.01 to N.32 connected to the west pylon in the north plane (cables not in the cable removal plane, but connected to the pylon from where cables were removed), Zone 2 with cables N.33 to N.64 connected to the east pylon in the north plane (cables not in the cable removal plane and not connected to the pylon from where cables were removed), Zone 3 with cables S.01 to S.32 connected to the west pylon in the south plane (cables in the cable removal plane and connected to the pylon from where

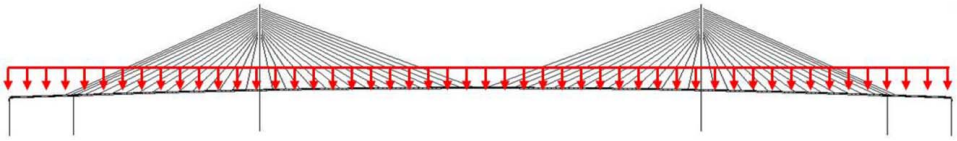

Fig. 11. Live load case.

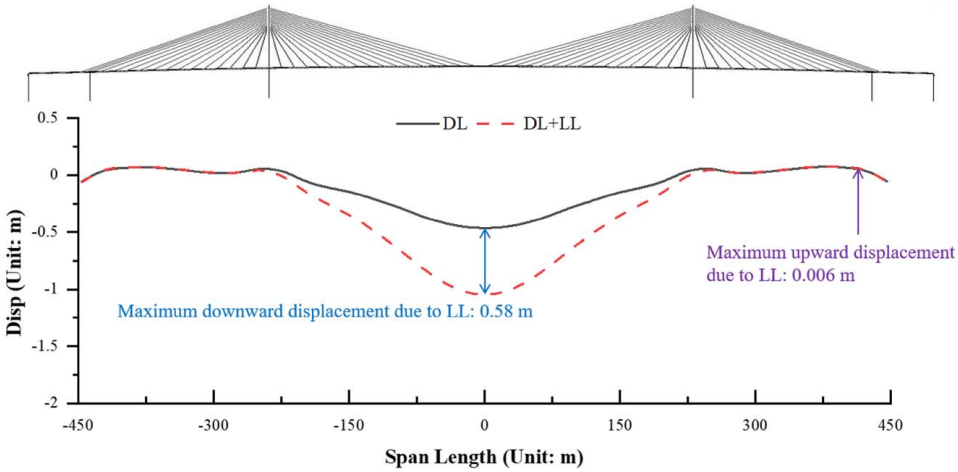

Fig. 12. Girder vertical deflection in the prototype bridge (unit: m).

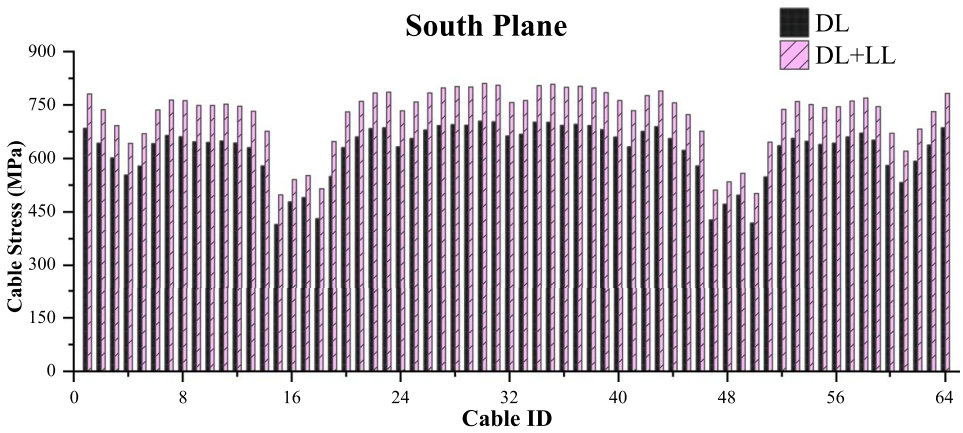

Fig. 13. Cable stresses under DL and DL + LL.

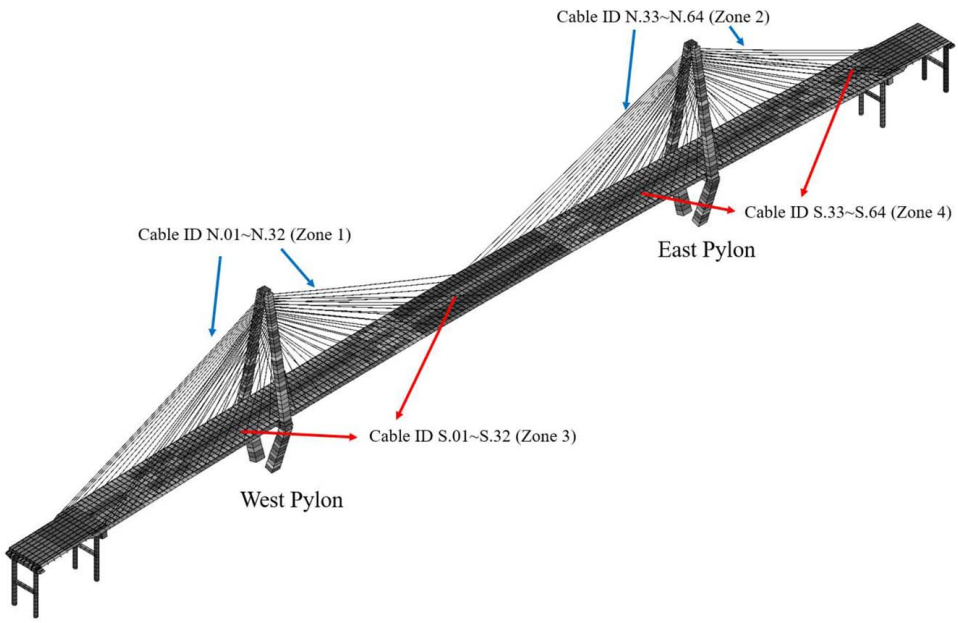

Fig. 14. Cable ID designation.

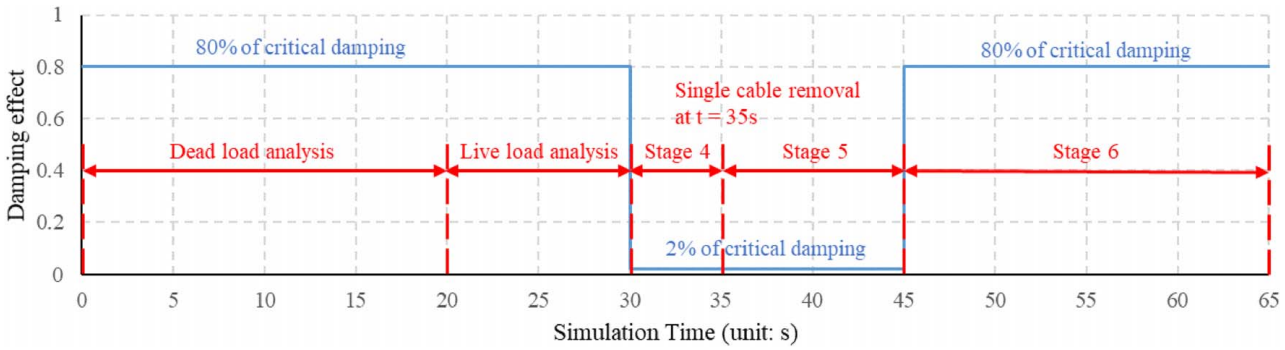

Fig. 15. Simulation stages and damping curve for single cable removal analysis.

cables were removed), Zone 4 with cables S.33 to S.64 connected to the east pylon in the south plane (cables in the cable removal plane and not connected to the pylon from where cables were removed).

Simulation Stages and Damping Effect

Member removal analysis was conducted through the following steps, as depicted in Fig. 15.

Stages 1–3: application of dead and live load effects until $t = 30$ s, as discussed earlier.

Stage 4: $t = 30$–35 s. The large global damping was adjusted back to a normal value once the vibrations due to load application subsided. The "normal" damping ratio was taken as 2% of critical damping, which is a representative value for long-span cable-stayed bridges (Narita and Yokoyama 1991).

Stage 5: $t = 35$–45 s. After the bridge reached its steady state under normal damping in Stage 4, a single cable was suddenly removed at $t = 35$ s, and immediately the bridge started to vibrate. This stage lasted for 10 s, which was deemed long enough to capture the peak response of the bridge based on extensive trial simulations with different durations.

Stage 6: $t = 45$–65 s. After the bridge vibrated for 10 s, the global damping was increased again to a large value (80% of critical damping) to damp out the vibrations rapidly so that the response could reach a new steady state. Numerous simulations suggested that this duration was sufficient for the bridge to reach its new steady state following the loss of a cable.

The time history of the bridge response, such as member force and displacement, during a single member loss can be categorized into three phases, as illustrated in Fig. 16. The steady-state response of the intact bridge is denoted as S_{intact}. Following the loss of a cable, the structural response achieves a peak value, denoted as $S_{\text{damage\_peak}}$. Following this, the amplitude of vibration is damped out to a new steady-state value of $S_{\text{damage\_steady}}$. Based on these response quantities, the behavior of the bridge during a cable loss event is assessed based on the following two indices: DCR and DAF. The definitions of these indices and results under different cable loss scenarios are presented next.

DCR

Three DCRs were computed as defined by

$$\text{DCR}_{\text{intact}} = \frac{\sigma_{\text{intact}}}{\sigma_y};\ \text{DCR}_{\text{damage\_peak}} = \frac{\sigma_{\text{damage\_peak}}}{\sigma_y};$$
$$\text{DCR}_{\text{damage\_steady}} = \frac{\sigma_{\text{damage\_steady}}}{\sigma_y} \quad (4)$$

where σ_{intact} = stress corresponding to dead and live loads on the bridge in the intact condition (without member loss); $\sigma_{\text{damage\_peak}}$ = peak stress following the sudden removal of a member; $\sigma_{\text{damage\_steady}}$ = steady-state stress after member removal; and σ_y = the yield stress. The preceding stresses were calculated from the axial cable forces divided by the cross-sectional area of the cables.

For each cable loss scenario, the DCRs were calculated for each intact cable and then the maximum value of DCR was identified. This process was repeated for sudden loss of different cables to obtain the DCR envelopes shown in Fig. 17 for $\text{DCR}_{\text{intact}}$, $\text{DCR}_{\text{damage\_peak}}$, and $\text{DCR}_{\text{damage\_steady}}$.

As shown in Fig. 17, most cables in the intact bridge had a $\text{DCR}_{\text{intact}}$ of approximately 0.45, except for DCRs of approximately 0.35 for cables near the pylons (i.e., cables 15–18 and 47–50 in both south and north planes). Since the removed cables (S.01 to S.32) were located in the south plane and attached to the west pylon, the envelope of $\text{DCR}_{\text{damage\_peak}}$ showed different trends in different zones. For cables in Zone 1, the envelope of $\text{DCR}_{\text{damage\_peak}}$ increased by 0.03–0.09 with respect to $\text{DCR}_{\text{intact}}$; for cables in Zone 2, the envelope $\text{DCR}_{\text{damage\_peak}}$ increased by 0.02–0.05 with respect to $\text{DCR}_{\text{intact}}$; for cables in Zone 3, which was the cable loss zone, the envelope of $\text{DCR}_{\text{damage\_peak}}$ increased by 0.07–0.28 with respect to $\text{DCR}_{\text{intact}}$; and for cables in Zone 4, the envelope of $\text{DCR}_{\text{damage\_peak}}$ increased by 0.02–0.08 with respect to $\text{DCR}_{\text{intact}}$. Typically, the value of $\text{DCR}_{\text{damage\_peak}}$ for cable S.18

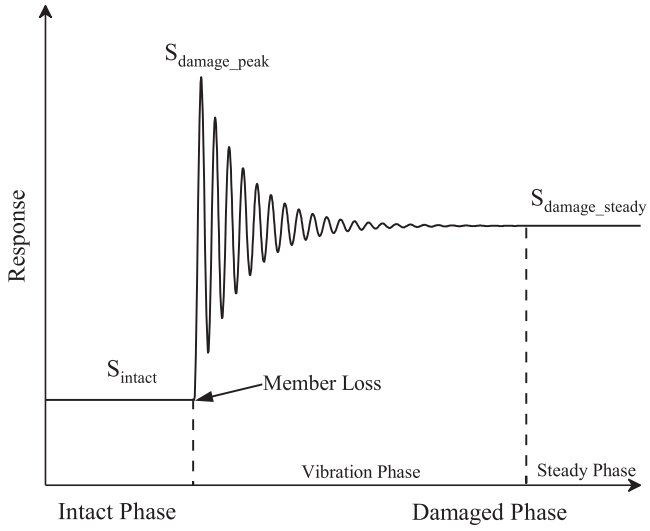

Fig. 16. Typical structure response time history under single member loss.

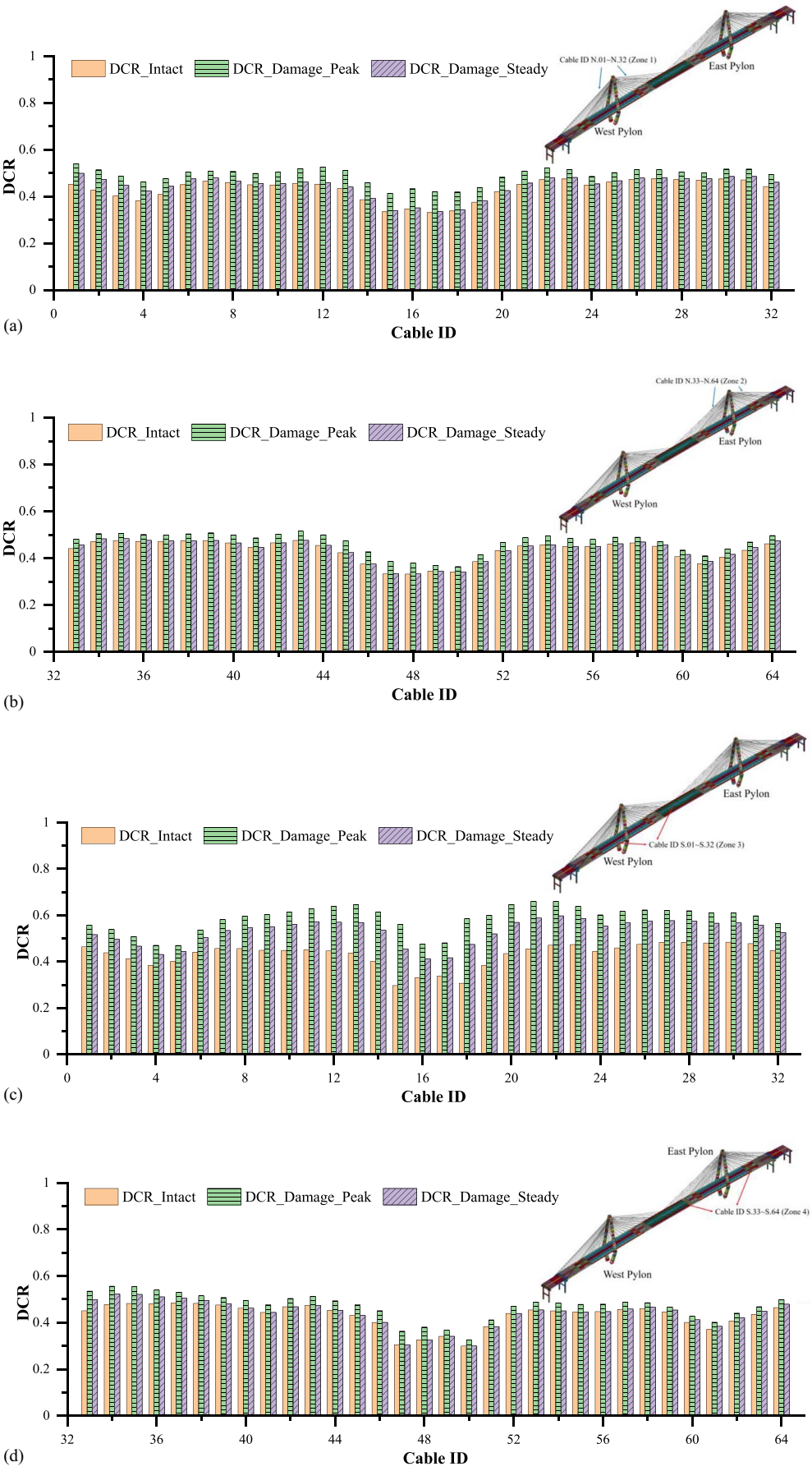

Fig. 17. Envelope of DCR for cable stress under DL + LL due to representative cable loss cases: (a) envelope of DCR for cable stress in Zone 1; (b) envelope of DCR for cable stress in Zone 2; (c) envelope of DCR for cable stress in Zone 3; and (d) envelope of DCR for cable stress in Zone 4.

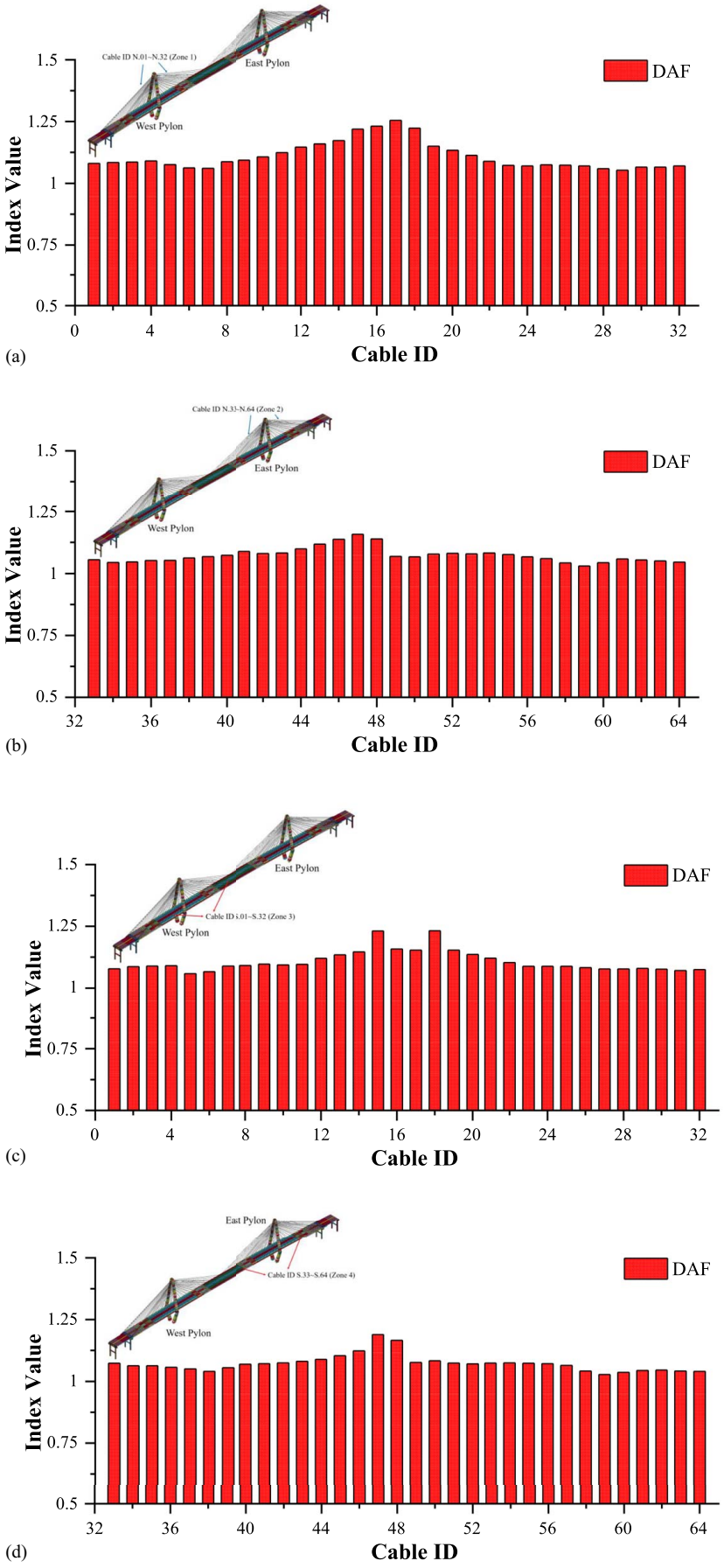

Fig. 18. Envelope of DAF for cable stress under DL + LL due to representative cable loss cases: (a) envelope of DAF for cable stress in Zone 1; (b) envelope of DAF for cable stress in Zone 2; (c) envelope of DAF for cable stress in Zone 3; and (d) envelope of DAF for cable stress in Zone 4.

Table 7. Cable loss scenarios of cable-stayed bridge

Scenario name	Lost cable no.
Cable Loss Scenario 1 (CLS 1) – Fig. 19	S.17 → S.18 → S.19 → S.20
Cable Loss Scenario 2 (CLS 2) – Fig. 22	S.32 → S.31 → …… → S.24 → S.23

increased to 0.58 from a value of $DCR_{intact} = 0.31$ and the maximum value of DCR_{damage_peak} occurred in cables S.21 and S.22 with a value of up to 0.66, indicating significant reserve capacity after the member loss event.

After the vibration caused by the loss of a single cable dissipated, the damaged bridge reached its new steady-state condition and there was a residual increased stress in the remaining cables. In the damaged state, the envelope of DCR_{damage_steady} showed different trends in different zones. For most cables in Zones 1, 2, and 4, the stress level in the damaged bridge returned to the level of the intact bridge, which indicates that a single cable loss event in one zone has limited effect on cables in the other zones. For some long cables in the Zone 1 (cables N.01 to N.04) and Zone 4 (cables S.33 and S35), the envelope of DCR_{damage_steady} increased slightly by 0.05 over DCR_{intact}. However, for cables in Zone 3, which was the cable loss zone, the envelope of DCR_{damage_steady} increased by 0.04–0.17 over DCR_{intact}. In particular, the DCR in cable S.18 almost doubled immediately after member removal (from 0.31 during the intact state to 0.58 for the peak vibration state) but then settled down to 0.47 in the damaged steady state. The maximum DCR_{damage_steady} in the damaged steady state occurred in cable S.22 with a value of 0.60. Given the relatively low DCR values, it is clear that the bridge is quite robust against single member removal.

DAF

The DAF is typically defined as a ratio between the dynamic response and the static response of a structure and can be calculated by Eq. (5) (Chopra 2012), while some researchers (Wolff and Starossek 2010) have also proposed Eq. (6) to calculate DAF for cable-supported structures under sudden cable loss as follows:

$$\mathrm{DAF} = \frac{S_{\mathrm{dynamic}}}{S_{\mathrm{static}}} = \frac{S_{\mathrm{damage\_peak}}}{S_{\mathrm{damage\_steady}}} \tag{5}$$

$$\mathrm{DAF} = \frac{S_{\mathrm{damage\_peak}} - S_{\mathrm{intact}}}{S_{\mathrm{damage\_steady}} - S_{\mathrm{intact}}} \tag{6}$$

However, DAF calculated by Eq. (6) sometimes results in unrealistic values. For example, if a bridge is subjected to a localized damage, structural members far from the damage will likely only be slightly affected. In this scenario, the $S_{\mathrm{damage\_steady}}$ is close to S_{intact} in these members, resulting in small denominators ($S_{\mathrm{damage\_steady}} - S_{\mathrm{intact}}$) in Eq. (6), thus leading to unrealistic DAF values for these members. Hence, Eq. (5) is used to calculate the DAF. The envelope of DAF for each cable under different cable loss event is shown in Fig. 18.

It is observed from Fig. 18 that, overall, DAF had a similar trend in all four zones. Based on 32 representative cable loss cases, the envelope of DAF in the four zones ranged from 1.05 to 1.25, 1.03 to 1.15, 1.06 to 1.23, and 1.03 to 1.19, respectively. The DAF values were slightly larger in Zones 1 and 3 in comparison to those in Zones 2 and 4, since the cables in Zones 1 and 3 are attached to the same pylon from which cables were removed. In addition, the DAF was slightly larger in the cables near the bridge pylons in all four zones. Analysis of the DAF results along with the low DCRs observed earlier confirm that the bridge is relatively insensitive to single cable removal.

Behavior of the Bridge under Multiple Cable Loss Events

The progressive collapse behavior of the bridge under multiple cable loss scenarios was analyzed under DL + LL. Similar to the process used for single cable removal analysis, the global damping constant was reduced to 2% of critical damping before the first cable was removed. The damping constant was then increased to a large value (80% of the critical damping) after a simulation time of 10 seconds (about four times the period of the first vibration mode), which was long enough to capture the peak response following the loss of the first cable. Once the bridge reached its new steady state, the global damping constant was reduced to 2% of critical once again prior to removing the second cable. This process was repeated for subsequent cable loss scenarios. The live load applied on the bridge was assumed constant during the entire multiple cable loss event. Two multiple cable loss scenarios were considered, which represent failure sequences in different parts of the bridge as shown in Table 7. The first, termed Cable Loss Scenario 1 (CLS 1) is shown in Fig. 19, while the second, designated CLS 2 is shown in Fig. 22.

Three limit states were established in order to evaluate the level of damage to the bridge: functionality limit state, member failure limit state, and ultimate limit state. The functionality limit state is defined as the damage level when tension cracks occurred in 10% of the deck area or the additional deflections from DL condition reached the limit of L/400 (JSCE 2007). The member failure limit state is defined as the damage level when a main structural member reached its yield point. The ultimate limit state is defined as the damage level when fracture occurred in a main structural member, or the entire bridge completely collapsed.

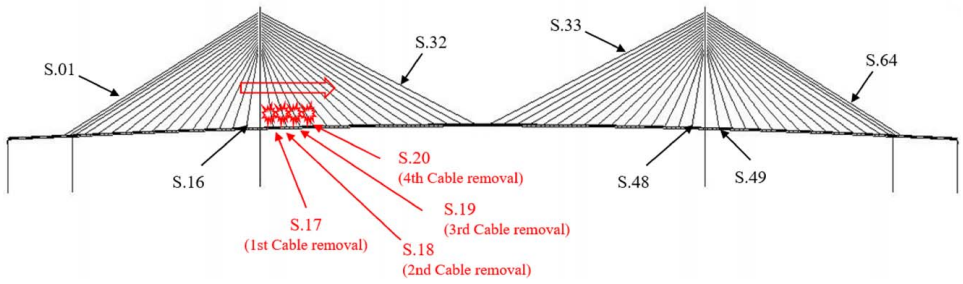

Fig. 19. Cable removal pattern in CLS 1.

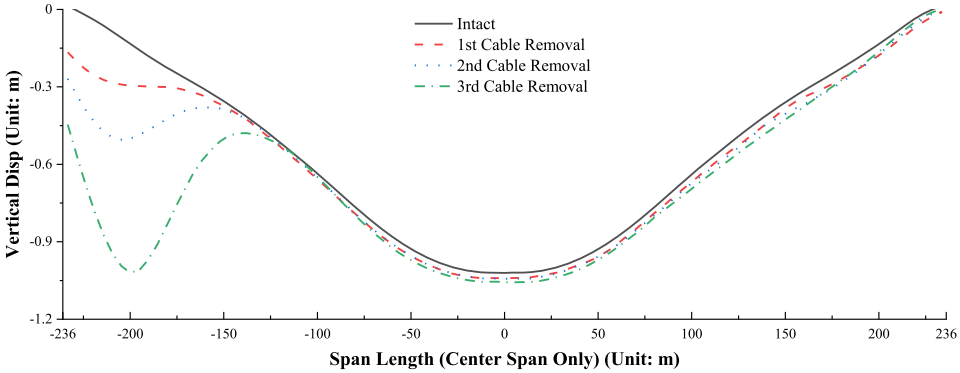

Fig. 20. Vertical displacements due to different cable removal in CLS 1.

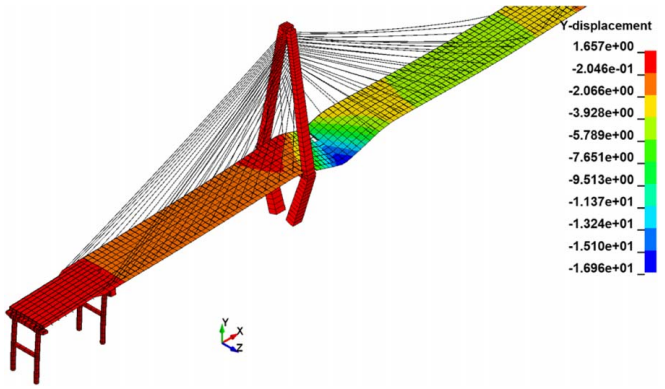

Fig. 21. Ultimate limit state after fourth cable loss (unit: m).

Progressive Collapse Behavior and Failure Modes during CLS 1

The main edge girder deformation in the center span due to CLS 1 is shown in Fig. 20.

Removal of First and Second Cables

Cable S.17 was the first cable removed at 35 s simulation time. The bridge's response reached steady-state behavior at 65 s. Following this, the second cable, cable S.18, was removed. The maximum vertical displacements along the edge girder in the center span during loss of cables S.17 and S.18 are shown in Fig. 20. The overall deformation after the loss of cable S.17 was almost the same as that of the intact bridge. However, close to the lost cable, the deformation increased by 0.152 m. After the loss of cable S.18, the deformation in the cable loss zone increased by another 0.152 m. The structural steel and stay cables remained elastic following these two cables loss events.

First Member Failure Limit State after Loss of the Third Cable

The third cable (cable S.19) was removed at 95 s simulation time. During the vibration of the bridge due to the loss of this cable, localized deflections increased suddenly to more than 0.914 m in the cable loss region, which was the largest deformation along the girder, as shown in Fig. 20. The maximum stress in the main edge girder was around 151.7 MPa before the loss of the third cable. After the cable loss event, the stress in the main girder in the cable loss region increased to more than 345 MPa and reached its yield limit.

Ultimate Limit State after the Loss of the Fourth Cable

The fourth cable (cable S.20) was removed at 125 s simulation time. During the vibration of the bridge due to sudden loss of this cable, two cables in the opposite plane (cables N.18 and N.19) reached their fracture strength. The lateral elastomeric bearings connecting the main girder member to the west pylon legs also suffered failure by reaching the failure criteria defined in Eqs. (2) and (3). The superstructure in the cable loss region collapsed and fell onto the pylon transverse beam where it was then supported, as shown in Fig. 21. The maximum vertical displacement in the cable loss region reached 16.7 m. At this point, the bridge reached its ultimate limit state, which in this case was collapse of a large portion of the bridge. Similar observations were made by Wolff and Starossek (2010). However, while the bridge pylon remained intact in CLS 1, it failed in bending in Wolff and Starossek (2010).

Progressive Collapse Behavior and Failure Modes during CLS 2

The CLS 2 process is illustrated in Fig. 22. The main edge girder deformation in the center span during the cable removal process is shown in Fig. 23. In this cable loss scenario, the displacements at

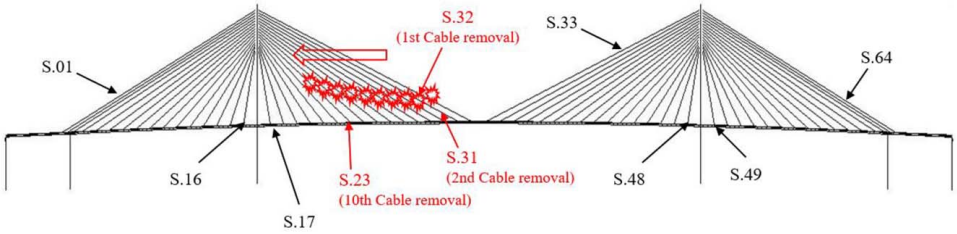

Fig. 22. Cable removal pattern in CLS 2.

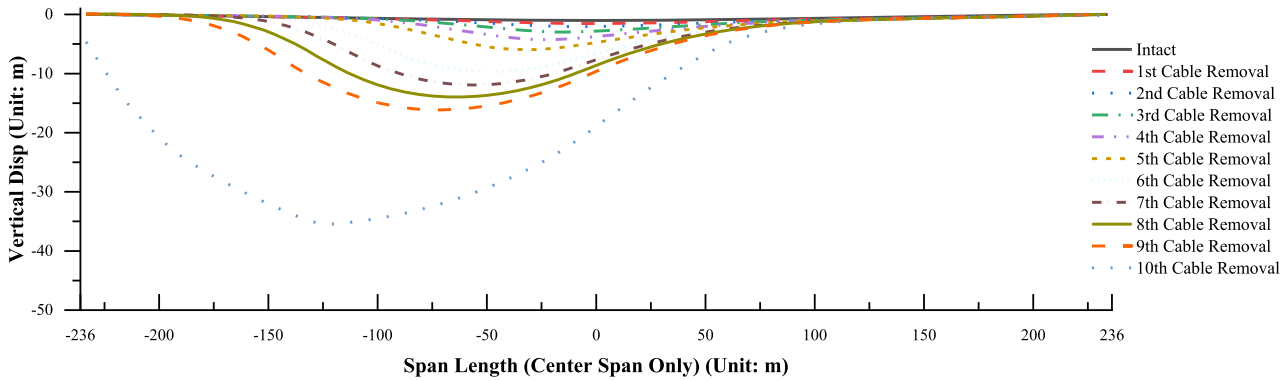

Fig. 23. Vertical displacements due to different cable removal in CLS 2.

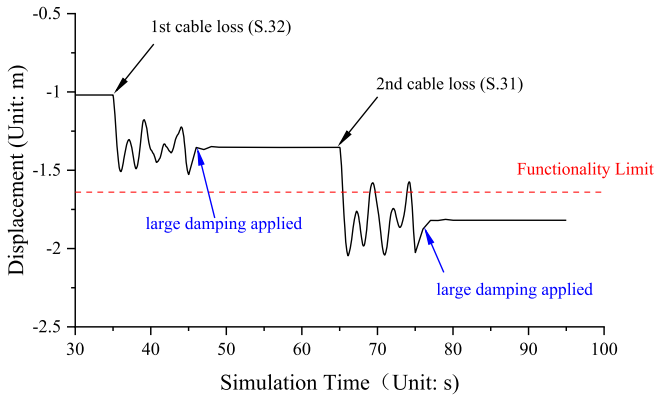

Fig. 24. Vertical displacement time history due to first two cables loss (unit: m).

the edge girder increased gradually as the cables were removed one by one until the tenth cable was removed. The displacements increased suddenly after the loss of the tenth cable as the bridge completely collapsed.

Functionality Limit State Exceeded after Loss of First and Second Cables

The first cable (cable S.32) was removed at 35 s simulation time and the bridge response reached steady-state conditions at 55 s simulation time. Following this, the second cable, cable S.31, was removed at 65 s simulation time. The maximum vertical displacement time history for the removal of the first two cables is shown in Fig. 24. As a result of the loss of the first cable, the downward displacement reached a peak of 1.52 m during the vibration of the bridge, which then became 1.37 m at the steady state. The maximum downward displacement reached 2.04 m during the vibration of the bridge due to loss of the second cable. At this point, the bridge exceeded its functionality limit state (i.e., L/400 = 1.64 m).

First Member Failure Limit State after Loss of the Third Cable

The third cable (cable S.30) was removed at 95 s simulation time. The maximum stress in the main edge girder was 291.0 MPa before the third cable was removed. After its removal, the stress in the main girder in the cable loss region reached its yield strength.

Severe Damage after the Loss of the Fifth Cable

The bridge did not reach any of the functionality limit states before progressive collapse occurred during CLS 1. However, it suffered severe damage with large global deflections during CLS 2. The fifth cable (cable S.28) was removed at 155 s simulation time. The vertical deformed shape after the fifth cables loss is shown in Fig. 25. It was observed that the bridge suffered large downward displacement near the cable loss location in this stage. In addition, the main structural members, such as girders and adjacent stayed

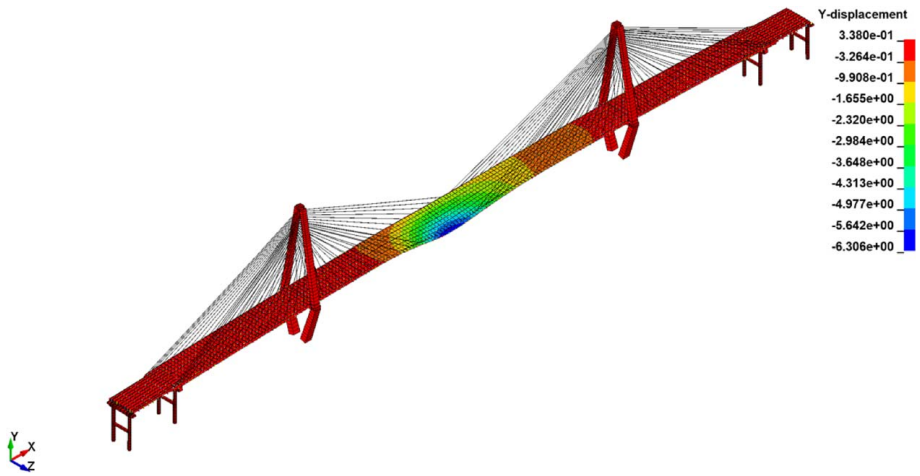

Fig. 25. Vertical deformation shape due to fifth cable loss (unit: m).

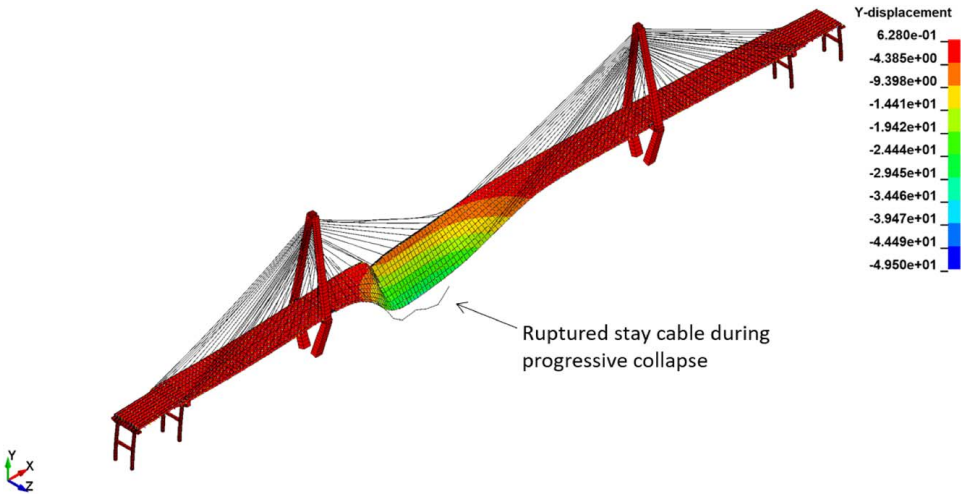

Fig. 26. Ultimate limit state after tenth cable loss (unit: m).

cables (cable S.27), reached their yield strength. Although seriously damaged, the bridge was not yet at incipient collapse.

Ultimate Limit State after Loss of the Tenth Cable

The tenth cable (cable S.22) was removed at 335 s simulation time. The adjacent cable (cable S.21) ruptured as a result. This was followed by rupture of cables S.20, S.19, and so on, thereby triggering an unzipping type of progressive collapse of the bridge. The ultimate limit state of the bridge was then reached as the bridge underwent complete collapse of the deck, as shown in Fig. 26. This type of progressive collapse was not seen in Wolff and Starossek (2010).

There are clear differences between CLS 1 and CLS 2. The bridge was more tolerant to the number of lost cables near its center span (10 cables) than near the pylon (four cables) before progressive collapse was triggered. It was also observed that the west pylon failed due to excessive unbalanced bending moment between the side span and the center under CLS 2 after progressive collapse was triggered, while the pylon still supported the collapsed superstructure in the cable loss region under CLS 1.

Conclusions

Computational simulation of a prototype cable-stayed bridge was used to investigate the behavior of the bridge to sudden cable loss through member removal analyses. Various single cable loss scenarios were modeled and two types of indices (DCR and DAF) were used to judge the effect of cable loss on system performance. The simulation results showed that only structural members in the vicinity of the removed cable, especially the adjacent cables in the same cable plane, were primarily affected by the dynamic effects associated with a single cable removal scenario. The DCRs of cables in the damaged bridges showed that all the cables and other main steel structural components were still in their elastic range after single cable removal. It was concluded that the bridge was quite robust against this type of scenario.

The behavior of the bridge subjected to multiple cable loss scenarios was also investigated. Specifically, the cables were removed one by one following the approach taken for single cable removal. During each cable removal step, the bridge was monitored closely, especially the response of the key structural parameters, such as vertical displacement of the bridge, stress in the main girder, and stress in adjacent stay cables. For CLS 1, the first member failure limit state was reached after loss of the third cable. The bridge suffered partial collapse after loss of the fourth cable. For CLS 2, the functionality limit state was reached after the loss of the second cable and first member failure was recorded after loss of the third cable. However, deformations remained small and the bridge exhibited robust behavior until loss of the fifth cable when severe damage was noted. It would take loss of another five cables (up to the tenth cable) for the bridge to reach collapse, at which point it failed by an unzipping type of progressive collapse that entailed progressive rupture of the adjacent cables. These results suggest the bridge is less tolerant to cable loss near its supporting pylons than its midspan.

Data Availability Statement

All the data, models, or code that support the findings of this study are available from the corresponding author upon reasonable request.

Acknowledgments

This material is based upon work supported by the Federal Highway Administration under contract number DTFH61-14-D-00010. Any opinions, findings, and conclusions or recommendations expressed in this publication are those of the authors and do not necessarily reflect the views of the Federal Highway Administration.

References

AASHTO. 2020. *AASHTO LRFD bridge design specifications. 9th ed*. Washington, DC: American Association of State Highway and Transportation Officials.

Agrawal, A. K., S. El-Tawil, Q. Chen, and H. Wang. 2022, In the press. *Redundancy in long span bridges for risk mitigation in a multi-hazard environment*. Washington, DC: Federal Highway Administration.

Alashker, Y., H. Li, and S. El-Tawil. 2011. "Approximations in progressive collapse modeling." *J. Struct. Eng.* 137 (9): 914–924. https://doi.org/10.1061/(ASCE)ST.1943-541X.0000452.

Aoki, Y., H. Valipour, B. Samali, and A. Saleh. 2013. "A study on potential progressive collapse responses of cable-stayed bridges." *Adv. Struct. Eng.* 16 (4): 689–706. https://doi.org/10.1260/1369-4332.16.4.689.

Bao, Y., S. K. Kunnath, S. El-Tawil, and H. S. Lew. 2008. "Macromodel-based simulation of progressive collapse: RC frame structures." *J. Struct. Eng.* 134 (7): 1070–1078. https://doi.org/10.1061/(ASCE)0733-9445(2008)134:7(1070).

Cai, J.-g., Y.-x. Xu, L.-p. Zhuang, J. Feng, and J. Zhang. 2012. "Comparison of various procedures for progressive collapse analysis of cable-stayed bridges." *J. Zhejiang Univ.-Sci. A* 13 (5): 323–334. https://doi.org/10.1631/jzus.A1100296.

Cao, R., A. K. Agrawal, and S. El-Tawil. 2020a. "Overheight impact on bridges: A computational case study of the Skagit River bridge collapse." *Eng. Struct.* 237: 112215. https://doi.org/10.1016/j.engstruct.2021.112215.

Cao, R., S. El-Tawil, and A. K. Agrawal. 2020b. "Miami pedestrian bridge collapse: Computational forensic analysis." *J. Bridge Eng.* 25 (1). 04019134. https://doi.org/10.1061/(ASCE)BE.1943-5592.0001532.

CEN (European Committee for Standardization). 2006. *Design of steel structures. Part 1.11: Design of structures with tension components*. Eurocode 3. Brussels, Belgium: CEN.

Chopra, A. K. 2012. *Dynamics of structures*. Upper Saddle River, NJ: Pearson Education.

Connor, R. J., F. J. Bonachera Martín, A. Varma, Z. Lai, and C. Korkmaz. 2018. *Fracture-critical system analysis for steel bridges (No. Project 12-87A)*. NCHRP Rep. No. 883. Washington, DC: Transportation Research Board.

Das, R., A. D. Pandey, M. J. Mahesh, P. Saini, and S. Anvesh. 2016. "Progressive collapse of a cable stayed bridge." *Procedia Eng.* 144: 132–139. https://doi.org/10.1016/j.proeng.2016.05.016.

DOD (Department of Defense). 2009. *Unified facilities criteria: Design of buildings to resist progressive collapse*. UFC 4-023-03. Herndon, VA: USDOD.

GSA (General Services Administration). 2003. *Progressive collapse analysis and design guidelines for new federal office buildings and major modernization projects*. Washington, DC: GSA.

Hyttinen, E., J. Valimaki, and E. Jarvenpaa. 1994. "Cable stayed bridges effect, of breaking of a cable." In Vol. 1994 of *Proc., Air Force Personnel Center Conf., Cable Stayed and Suspension Bridges*, 303–311.Paris, France: AFPC.

JSCE (Japan Society of Civil Engineers). 2007. *Standard specifications for steel and composite structures*. Tokyo: JSCE.

Kao, C. S., and C. H. Kou. 2010. "The influence of broken cables on the structural behavior of long-span cable-stayed bridges." *J. Mar. Sci. Technol.* 18 (3): 395–404.

Kawai, Y., D. Siringoringo, and Y. Fujino. 2014. "Failure analysis of the hanger clamps of the Kutai-Kartanegara Bridge from the fracture mechanics viewpoint." *J. JSCE* 2 (1): 1–6. https://doi.org/10.2208/journalofjsce.2.1_1.

Kent, D. C., and R. Park. 1971. "Flexural members with confined concrete." *J. Struct. Div.* 97 (7): 1969–1990. https://doi.org/10.1061/JSDEAG.0002957.

Khandelwal, K., S. El-Tawil, S. K. Kunnath, and H. S. Lew. 2008a. "Macromodel-based simulation of progressive collapse: Steel frame structures." *J. Struct. Eng.* 134 (7): 1070–1078. https://doi.org/10.1061/(ASCE)0733-9445(2008)134:7(1070).

Khandelwal, K., S. El-Tawil, and F. Sadek. 2008b. "Progressive collapse analysis of seismically designed steel braced frames." *J. Constr. Steel Res.* 65 (3): 699–708. https://doi.org/10.1016/j.jcsr.2008.02.007.

LSTC (Livermore Software Technology Corporation). 2020. "LS-DYNA® keywords user manual Volume I-Keyword." Accessed September 9, 2020. https://www.dynasupport.com/manuals/ls-dyna-manuals/ls -dyna_manual_volume_i_r12.pdf.

Mozos, C. M., and A. C. Aparicio. 2010a. "Parametric study on the dynamic response of cable stayed bridges to the sudden failure of a stay, Part I: Bending moment acting on the deck." *Eng. Struct.* 32 (10): 3288–3300. https://doi.org/10.1016/j.engstruct.2010.07.003.

Mozos, C. M., and A. C. Aparicio. 2010b. "Parametric study on the dynamic response of cable stayed bridges to the sudden failure of a stay, Part II: Bending moment acting on the pylons and stress on the stays." *Eng. Struct.* 32 (10): 3301–3312. https://doi.org/10.1016/j.engstruct.2010.07.002.

Narita, N., and K. Yokoyama. 1991. "A summarized account of damping capacity and measures against wind action in cable-stayed bridges in Japan." *Cable-stayed bridges: Recent developments and their future*, 257–278. Amsterdam, Netherlands: Elsevier.

PTI (Post-Tensioning Institute). 2006. *Post-tensioning manual*. 6th ed. Phoenix, AZ: Post-Tensioning Institute.

PTI (Post-Tensioning Institute). 2007. *Recommendations for stay cable design, testing and installation*. 4th ed. Phoenix, AZ: Post-Tensioning Institute.

TTSB (Taiwan Transportation Safety Board). 2020. *Final report on Nanfangao sea-crossing bridge collapse*. Rep. No. TTSB-HOR-20-11-001. Taipei, Taiwan: TTSB.

Vecchio, F. J., and W. Shim. 2004. "Experimental and analytical reexamination of classic concrete beam tests." *J. Struct. Eng.* 130 (3): 460–469. https://doi.org/10.1061/(ASCE)0733-9445(2004)130:3(460).

Wolff, M., and U. Starossek. 2010. "Cable-loss analyses and collapse behavior of cable-stayed bridges." In *Proc., 5th Int. Conf., International Association for Bridge Maintenance and Safety, Management and Life-Cycle Optimization*, 2179–2186. Boca Raton, FL: CRC Press.

Zhou, Y., and S. Chen. 2015. "Numerical investigation of cable breakage events on long-span cable-stayed bridges under stochastic traffic and wind." *Eng. Struct.* 105: 299–315. https://doi.org/10.1016/j.engstruct.2015.07.009.

Zoli, T. P., and R. Woodward. 2005. "Design of long span bridges for cable loss." In Vol. 90 of *Proc., Int. Association for Bridge and Structural Engineering Symp. Report*, 17–25. Zurich, Switzerland: International Association for Bridge and Structural Engineering (IABSE).

Zoli, T. P., and J. Steinhouse. 2007. "Some considerations in the design of long span bridges against progressive collapse." In *Proc., 23rd US-Japan Bridge Engineering Workshop*. Tsukuba, Japan: Public Works Research Institute.